

# SUPPORTING INFORMATION

## Crystallographically Textured Nanomaterials Produced from the Liquid Phase Sintering of $\text{Bi}_x\text{Sb}_{2-x}\text{Te}_3$ Nanocrystal Building Blocks

Yu Liu,<sup>†</sup> Yu Zhang,<sup>†</sup> Silvia Ortega,<sup>†</sup> Maria Ibáñez,<sup>‡,§</sup> Khak Ho Lim,<sup>⊥</sup> Albert Grau-Carbonell,<sup>//</sup> Sara Martí-Sánchez,<sup>//</sup> Ka Ming Ng,<sup>⊥</sup> Jordi Arbiol,<sup>//, #</sup> Maksym V. Kovalenko,<sup>‡,§</sup> Doris Cadavid,<sup>†,¶,\*</sup> and Andreu Cabot<sup>†,#,\*</sup>

<sup>†</sup> Catalonia Energy Research Institute - IREC, Sant Adria de Besòs, 08930 Barcelona, Spain.

<sup>‡</sup> Institute of Inorganic Chemistry, Department of Chemistry and Applied Biosciences, ETH Zürich, Vladimir Prelog Weg 1, CH-8093, Switzerland.

<sup>§</sup> Empa-Swiss Federal Laboratories for Materials Science and Technology, Dübendorf, Überlandstrasse 129, CH-8600, Switzerland.

<sup>⊥</sup> Department of Chemical and Biological Engineering, Hong Kong University of Science and Technology, Clear Water Bay Hong Kong.

<sup>//</sup> Catalan Institute of Nanoscience and Nanotechnology (ICN2), CSIC and BIST, Campus UAB, Bellaterra, 08193 Barcelona, Catalonia, Spain.

<sup>#</sup> ICREA, Pg. Lluís Companys 23, 08010 Barcelona, Spain.

<sup>¶</sup> Departamento de Física, Universidad Nacional de Colombia, 111321 Ciudad Universitaria, Bogotá, Colombia.

\* *E-mails:* D. Cadavid: [dycadavidr@unal.edu.co](mailto:dycadavidr@unal.edu.co)  
A. Cabot: [acabot@irec.cat](mailto:acabot@irec.cat)

## Contents

1. Chemicals and solvents.....	3
2. Synthesis of $\text{Bi}_x\text{Sb}_{2-x}\text{Te}_3$ nanoplatelets.....	3
3. Synthesis of tellurium and $\text{Bi}_2\text{Te}_3$ nanowires.....	3
4. Bulk nanomaterial consolidation .....	4
5. Structural and chemical characterization .....	4
6. Thermoelectric property measurements.....	4
7. Crystal structure .....	5
8. $\text{Bi}_x\text{Sb}_{2-x}\text{Te}_3$ building blocks.....	5
9. Composition of $\text{Bi}_x\text{Sb}_{2-x}\text{Te}_3$ nanoplatelets.....	6
10. HRTEM and STEM-EELS characterization.....	7
11. Schematic illustration of samples used to measure thermoelectric properties.....	8
12. Effect of the excess of tellurium on the pellet anisotropy.....	9
13. $\text{Bi}_2\text{Te}_3$ nanowires as initial building blocks .....	10
14. Commercial $\text{Bi}_{0.5}\text{Sb}_{1.5}\text{Te}_3$ ingot.....	12
15. Tellurium spilling.....	13
16. One press and release step .....	13
17. Composition optimization.....	15
18. Additional thermoelectric properties .....	16
19. Average values and maximum efficiency .....	19
20. Literature comparison .....	20
21. Stability.....	21
22. Repeatability .....	22
23. References.....	24

## 1. Chemicals and solvents

Bismuth (III) nitrate pentahydrate ( $\text{Bi}(\text{NO}_3)_3 \cdot 5\text{H}_2\text{O}$ ,  $\geq 99.99\%$ ), bismuth (III) chloride ( $\text{BiCl}_3$ ,  $\geq 99\%$ ), antimony (III) chloride ( $\text{SbCl}_3$ , 99%), potassium hydroxide ( $\text{KOH}$ ,  $\geq 98\%$ ), Polyvinylpyrrolidone ( $((\text{C}_6\text{H}_9\text{NO})_n$ , average mol wt  $\sim 55,000$ ), tellurium dioxide ( $\text{TeO}_2$ ,  $\geq 99\%$ ), hydrazine monohydrate ( $\text{NH}_2\text{NH}_2 \cdot \text{H}_2\text{O}$ , 64~65%) and diethylene glycol ( $(\text{HOCH}_2\text{CH}_2)_2\text{O}$ , DEG,  $\geq 99\%$ ) were purchased from Sigma Aldrich. Sodium tellurite ( $\text{Na}_2\text{TeO}_3$ , 99.5%) and ethylene glycol ( $\text{HOCH}_2\text{CH}_2\text{OH}$ , EG, 99%) were purchased from Fisher. Analytical grade acetone and ethanol were obtained from various sources. All chemicals were used as received, without further purification.

## 2. Synthesis of $\text{Bi}_x\text{Sb}_{2-x}\text{Te}_3$ nanoplatelets

To produce around 5 g of  $\text{Bi}_x\text{Sb}_{2-x}\text{Te}_3$  ( $x = 0, 0.4, 0.5$  and  $0.6$ ) nanoplatelets with a nominal 25% mol excess tellurium,  $7.2x$  mmol of  $\text{Bi}(\text{NO}_3)_3 \cdot 5\text{H}_2\text{O}$ ,  $[7.2 \cdot (2-x)]$  mmol of  $\text{SbCl}_3$ , 27 mmol  $\text{Na}_2\text{TeO}_3$ , 72 mmol  $\text{KOH}$  and 1.44 g PVP as stabilizing agent were dissolved in 280 mL DEG in a 500 mL three-neck flask. The mixture was stirred under argon atmosphere at room temperature for 20 min. Then the solution was heated to  $190^\circ\text{C}$ , and during the heating up, at  $110^\circ\text{C}$ , 10.8 mL hydrazine monohydrate was swiftly injected. Upon hydrazine injection, the color of the solution immediately changed from slightly brown to dark. The mixture was kept at  $190^\circ\text{C}$  for 4 h and then it was naturally cooled to room temperature by removing the heating mantle. The solid product was collected by adding acetone to the solution and centrifuging it. In a second step, ethanol was used to redisperse the particles and acetone ( $V_{\text{ethanol}}/V_{\text{acetone}} = 1:2$ ) to precipitate them again. In a third step, deionized water was added to solubilize remaining impurities and nanoparticles were precipitated by slow centrifugation. This procedure was repeated twice. In a last step, particles were redispersed with ethanol and precipitated with acetone, like in step two. Finally, particles were dried under vacuum at room temperature. This synthesis protocol was optimized to produce more than 5 g of nanoplatelets per batch, which was the amount required for a complete characterization of the material at the laboratory scale.

## 3. Synthesis of tellurium and $\text{Bi}_2\text{Te}_3$ nanowires

Tellurium and  $\text{Bi}_2\text{Te}_3$  nanowires were prepared following the approach developed by Yue Wu et al.<sup>1</sup> In a typical synthesis of tellurium nanowires, 5.6 mmol of  $\text{TeO}_2$ , 37 mmol of  $\text{KOH}$ , 1.5 g of PVP, and 56 mL of EG were added into a 250 mL three-neck flask. The mixture was stirred and heated to  $140^\circ\text{C}$ . At this temperature, 0.87 mL of a 64~65%  $\text{N}_2\text{H}_4 \cdot \text{H}_2\text{O}$  solution were injected into the flask. The reaction mixture was maintained at  $140^\circ\text{C}$  for 1 h to allow all tellurium to be reduced.

$\text{Bi}_2\text{Te}_3$  nanowires were produced by adding bismuth to the just formed tellurium nanowires produced as described in the previous paragraph. Briefly, after 1 h of reaction at  $140^\circ\text{C}$  to form the tellurium nanowires, the temperature of the solution was raised to  $160^\circ\text{C}$ . At this point, a hot  $\text{BiCl}_3/\text{EG}$  solution was injected into the flask. This  $\text{BiCl}_3/\text{EG}$  solution was produced by adding 3.6 mmol of  $\text{BiCl}_3$  into 15 mL of EG in a glass vial that was heated to  $100\text{--}120^\circ\text{C}$ . The  $\text{BiCl}_3/\text{EG}$  solution was allowed to react with the tellurium nanowires for 1 h at  $160^\circ\text{C}$ . Then, the solution was naturally cooled to room temperature. Both, tellurium and  $\text{Bi}_2\text{Te}_3$  nanowires were purified using the same procedure as described above for  $\text{Bi}_x\text{Sb}_{2-x}\text{Te}_3$  nanocrystals.

#### 4. Bulk nanomaterial consolidation

Dried  $\text{Bi}_x\text{Sb}_{2-x}\text{Te}_3$  ( $x=0.4, 0.5$  and  $0.5$ ) nanoplatelets were annealed at  $350^\circ\text{C}$  for 60 min under an argon flow inside a tube furnace. The annealed particles, in the form of a powder, were loaded into a graphite die and compacted into cylinders ( $\varnothing 10\text{ mm}\times 10\text{ mm}$ ) in an argon atmosphere using a custom-made hot press. The hot press temperature was set at  $480^\circ\text{C}$  and pressure to 80 MPa and the amount of time that the material was kept in these conditions was 210 s. From these cylinders, rectangular bars of about  $8 \times 6 \times 1\text{ mm}^3$  were cut in two directions, along the press axis and within the plane normal to this axis. The relative densities of the compacted pellets were measured by the Archimedes' method and found to be around 94% of the theoretical value, when materials with an excess of tellurium were hot pressed in these conditions.

#### 5. Structural and chemical characterization

X-ray diffraction (XRD,  $2\theta$ :  $20^\circ$  to  $80^\circ$ ; scanning rate:  $5^\circ/\text{min}$ ) analyses were carried out on a Bruker AXS D8 ADVANCE X-ray diffractometer with  $\text{Cu-K}\alpha$  radiation ( $\lambda = 1.5406\text{ \AA}$ ). Size and morphology of the initial nanoparticles and the consolidated materials were examined by transmission electron microscopy (TEM) using a ZEISS LIBRA 120, operating at 120 kV and field-emission scanning electron microscopy (SEM) using a Zeiss Auriga at 5.0 kV. High resolution TEM (HRTEM) micrographs were obtained using a Tecnai F20 field-emission gun microscope with a 0.19 nm point-to-point resolution at 200 keV with an embedded Gatan QUANTUM image filter for EELS analyses. Compositions were analyzed using an Oxford energy dispersive X-ray spectrometer (EDX) attached to the Zeiss Auriga SEM at 20.0 kV. TGA-DSC was done using the NETZSCH STA 409 C/CD Instrument in the temperature range from  $40^\circ\text{C}$  to  $900^\circ\text{C}$  with a heating rate of  $3.0\text{ K/min}$  under argon atmosphere.

#### 6. Thermoelectric property measurements

Seebeck coefficients were measured using a static DC method. Electrical resistivity data was obtained by a standard four-probe method. Both the Seebeck coefficient and the electrical resistivity were measured simultaneously in a LSR-3 LINSEIS system in the temperature range between room temperature and 498 K under helium atmosphere. All samples were measured at least 3 consecutive times during heating up to around 498 K. Taking into account the system accuracy and the measurement precision, an error of ca. 4 % in the measurement of the electrical conductivity and Seebeck coefficient was estimated. Thermal conductivities ( $\kappa_{total}$ ) were calculated from the thermal diffusivity ( $\lambda$ ), the heat capacity ( $C_p$ ) and the mass density of the material ( $\rho$ ), using  $\kappa_{total} = \lambda C_p \rho$ . A Xenon Flash Apparatus XFA600 was used to determine the thermal diffusivities of the samples with an estimated error of ca. 5 %. The constant pressure heat capacity was estimated from empirical formulas by the Dulong–Petit limit (3R law). The density values were calculated using the Archimedes' method. To avoid cluttering the plots, error bars were not included in the figures. The Hall carrier concentration ( $n$ ) and mobility ( $\mu$ ) at room temperature (298 K) were measured with a Physical Property Measurement System (PPMS-9T, 10 % error, Quantum Design Inc., USA) using a magnetic field of 2 T. Values provided correspond to the average of 5 consecutive measurements.

## 7. Crystal structure

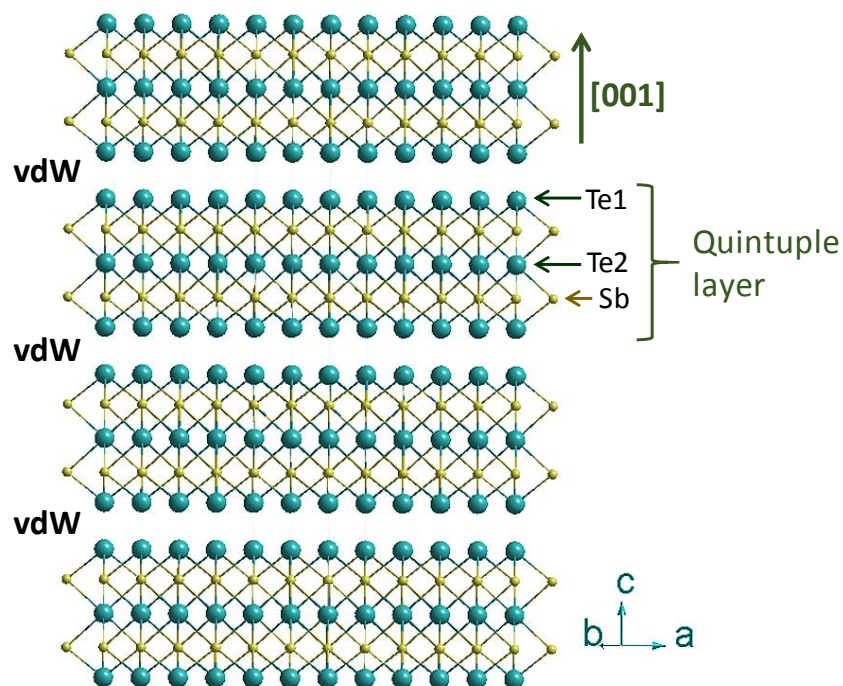


**Figure S1.** Crystal structure of  $\text{Sb}_2\text{Te}_3$ .

## 8. $\text{Bi}_x\text{Sb}_{2-x}\text{Te}_3$ building blocks

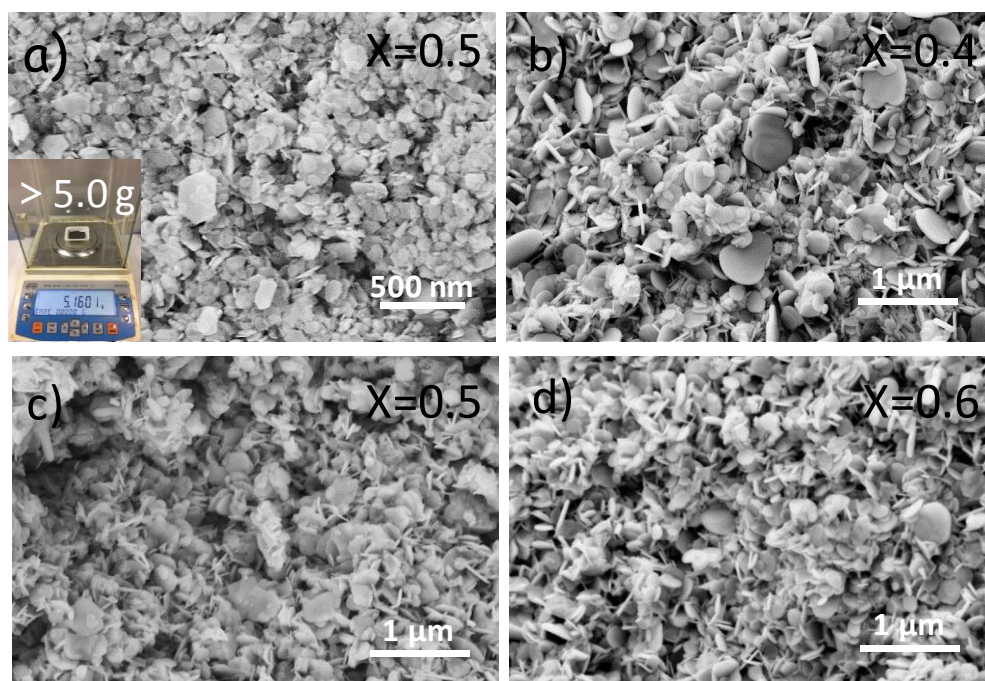


**Figure S2.** a) SEM image of  $\text{Bi}_{0.5}\text{Sb}_{1.5}\text{Te}_3$  nanoplatelets with 25% excess of tellurium. Inset shows the amount of NCs produced per batch. b-d) SEM images of  $\text{Bi}_x\text{Sb}_{2-x}\text{Te}_3$  ( $x=0.4, 0.5$  and  $0.6$ ) nanoplatelets with 25% excess tellurium after annealing at 350  $^\circ\text{C}$  for 1 h.

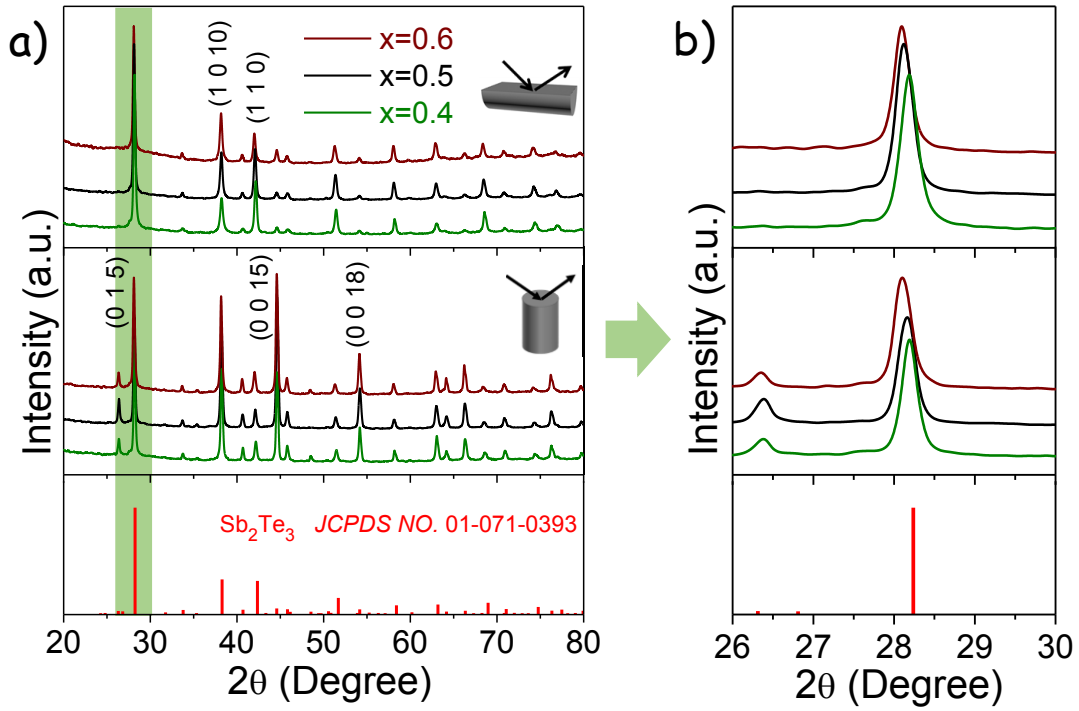


**Figure S3.** a) XRD patterns of consolidated  $\text{Bi}_x\text{Sb}_{2-x}\text{Te}_3$  ( $x=0.4, 0.5$  and  $0.6$ ) pellets measured in the two directions, parallel and normal to the press direction. b) Detail of the same XRD patterns showing the systematic shift of the (0 1 5) peak with the bismuth composition ( $x$ ).

## 9. Composition of $\text{Bi}_x\text{Sb}_{2-x}\text{Te}_3$ nanoplatelets

**Table S1.** SEM-EDX composition of the initial  $\text{Bi}_x\text{Sb}_{2-x}\text{Te}_3$  ( $X=0.4, 0.5$  and  $0.6$ ) nanoplatelets containing an excess of tellurium.

Element	$x=0.4$	$x=0.5$	$x=0.6$
Bi	0.43	0.52	0.61
Sb	1.57	1.48	1.39
Te	3.42	3.26	3.38
total	$\text{Bi}_{0.43}\text{Sb}_{1.57}\text{Te}_{3.42}$	$\text{Bi}_{0.52}\text{Sb}_{1.48}\text{Te}_{3.26}$	$\text{Bi}_{0.61}\text{Sb}_{1.39}\text{Te}_{3.38}$

**Table S2.** SEM-EDX composition of the  $\text{Bi}_x\text{Sb}_{2-x}\text{Te}_3$  ( $X=0.4, 0.5$  and  $0.6$ ) powders containing an excess of tellurium, after annealing at  $350^\circ\text{C}$  for 60 min.

Element	$x=0.4$	$x=0.5$	$x=0.6$
Bi	0.42	0.52	0.60
Sb	1.54	1.48	1.39
Te	3.39	3.25	3.33
total	$\text{Bi}_{0.42}\text{Sb}_{1.54}\text{Te}_{3.39}$	$\text{Bi}_{0.52}\text{Sb}_{1.48}\text{Te}_{3.25}$	$\text{Bi}_{0.60}\text{Sb}_{1.39}\text{Te}_{3.33}$



**Table S3.** SEM-EDX Composition of the  $\text{Bi}_x\text{Sb}_{2-x}\text{Te}_3$  ( $x=0.4, 0.5$  and  $0.6$ ) pellets after consolidation at  $480^\circ\text{C}$  for 210 s.

Element	x=0.4	x=0.5	x=0.6
Bi	0.41	0.53	0.61
Sb	1.57	1.47	1.38
Te	3.03	2.96	2.97
total	$\text{Bi}_{0.41}\text{Sb}_{1.57}\text{Te}_{3.03}$	$\text{Bi}_{0.53}\text{Sb}_{1.47}\text{Te}_{2.96}$	$\text{Bi}_{0.61}\text{Sb}_{1.38}\text{Te}_{2.97}$

## 10. HRTEM and STEM-EELS characterization

In order to study the crystal structure of the pellets, we obtained cross-sectional samples by using conventional mechanical thinning and ion milling. High resolution transmission electron microscopy (HRTEM) analyses such as those shown in Figures S4 and S5 show the layered structure of a  $\text{Bi}_{0.5}\text{Sb}_{1.5}\text{Te}_3$  pellet. The material was found to crystallize in the monoclinic C12-M phase with lattice constants  $a=15.705\text{ \AA}$ ,  $b=4.305\text{ \AA}$ ,  $c=9.395\text{ \AA}$ ,  $\alpha=\gamma=90.00^\circ$  and  $\beta=90.05^\circ$ ,<sup>2</sup> presenting a layered pattern along the c-axis as commonly found in  $\text{Bi}_2\text{Te}_3$ <sup>3</sup> or other  $\text{Bi}_x\text{Sb}_{2-x}\text{Te}_3$  composites.<sup>4</sup> Notice that in the later cases, the structure tends to crystallize in the trigonal R3-M structure instead of the monoclinic C12-M found here. Nevertheless, both structures show clear layered patterns along the c-axis. Compositional analyses were performed with STEM-EELS. Bi, Te and Sb were found to be homogeneously distributed through the pellet.

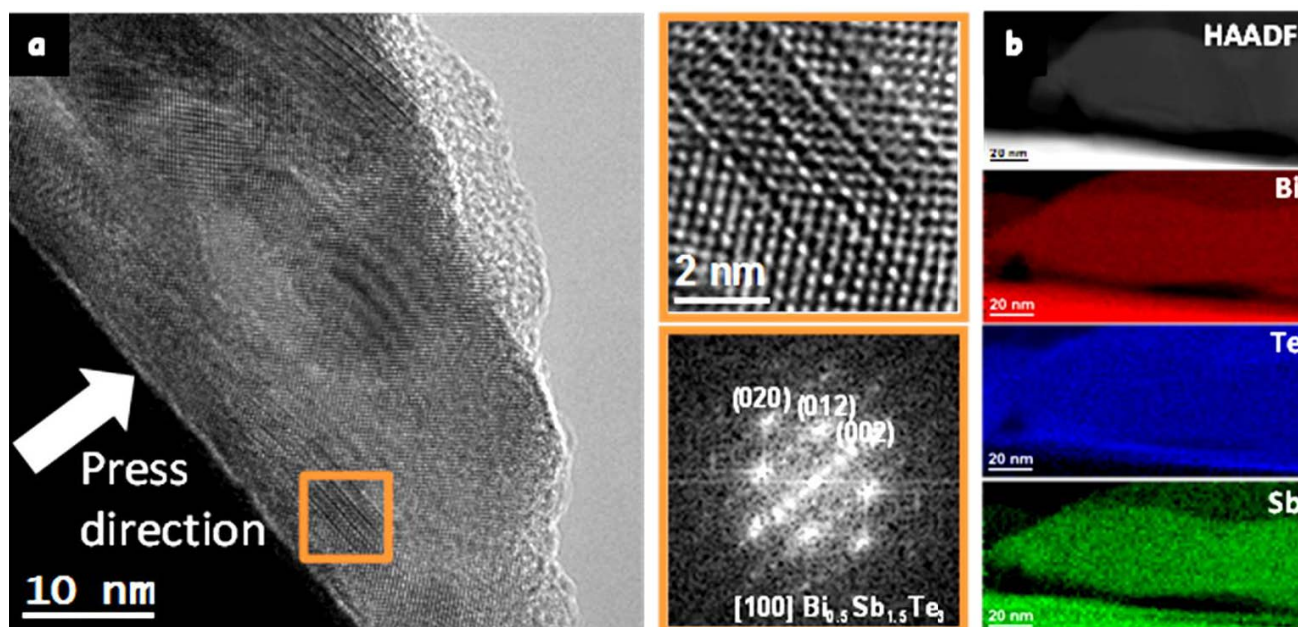


**Figure S4.** a) HRTEM micrograph obtained on a region of the pellet showing the multiple layered structure of the  $\text{Bi}_{0.5}\text{Sb}_{1.5}\text{Te}_3$  along its  $[100]$  zone axis. The region observed presents several crystalline domains oriented along the basal planes. Details of the squared area and the corresponding indexed power spectrum are also shown. Notice that the structure present stacking faults. b) Areal density of

Bi, Te and Sb obtained through STEM-EELS signal integration after background removal using Bi (N-edge), Te (M-edge) and Sb (M-edge), respectively.

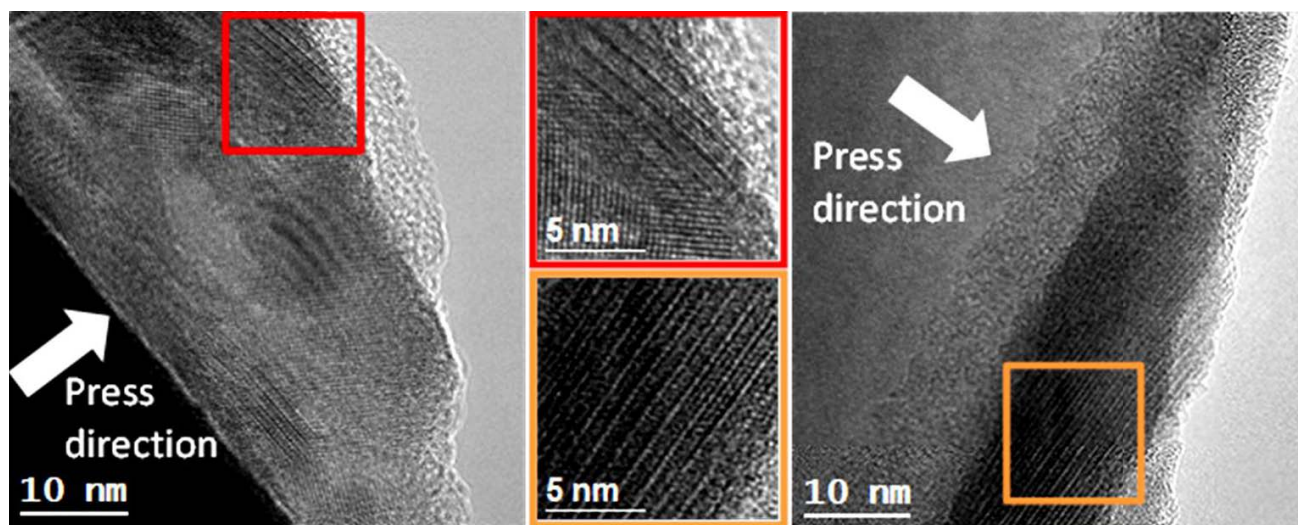


**Figure S5.** HRTEM micrographs of two areas within the pellet cross section showing the layered monoclinic structure of  $\text{Bi}_{0.5}\text{Sb}_{1.5}\text{Te}_3$  along its  $[100]$  zone axis.

## 11. Schematic illustration of samples used to measure thermoelectric properties

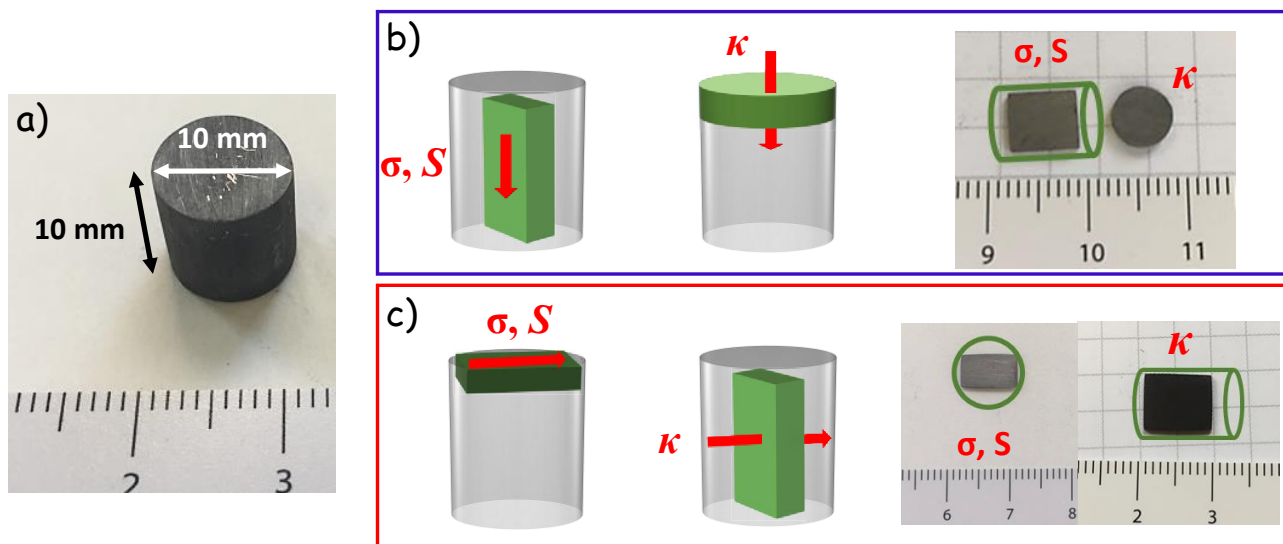


**Figure S6.** a) Photograph of one of the cylindrical pellets produced by hot pressing and to measure the thermoelectric properties of the materials in the two directions. b-c) Schematic illustrations and photographs of the samples obtained from the cylindrical pellets and used to measure thermoelectric properties in both directions, parallel (b) and normal (c) to the press direction. Electrical conductivities and Seebeck coefficients were always measured using rectangular samples. Thermal conductivities were measured from disk-shaped samples in the direction of the press axis and from rectangular samples in the direction normal to the press axis.



## 12. Effect of the excess of tellurium on the pellet anisotropy

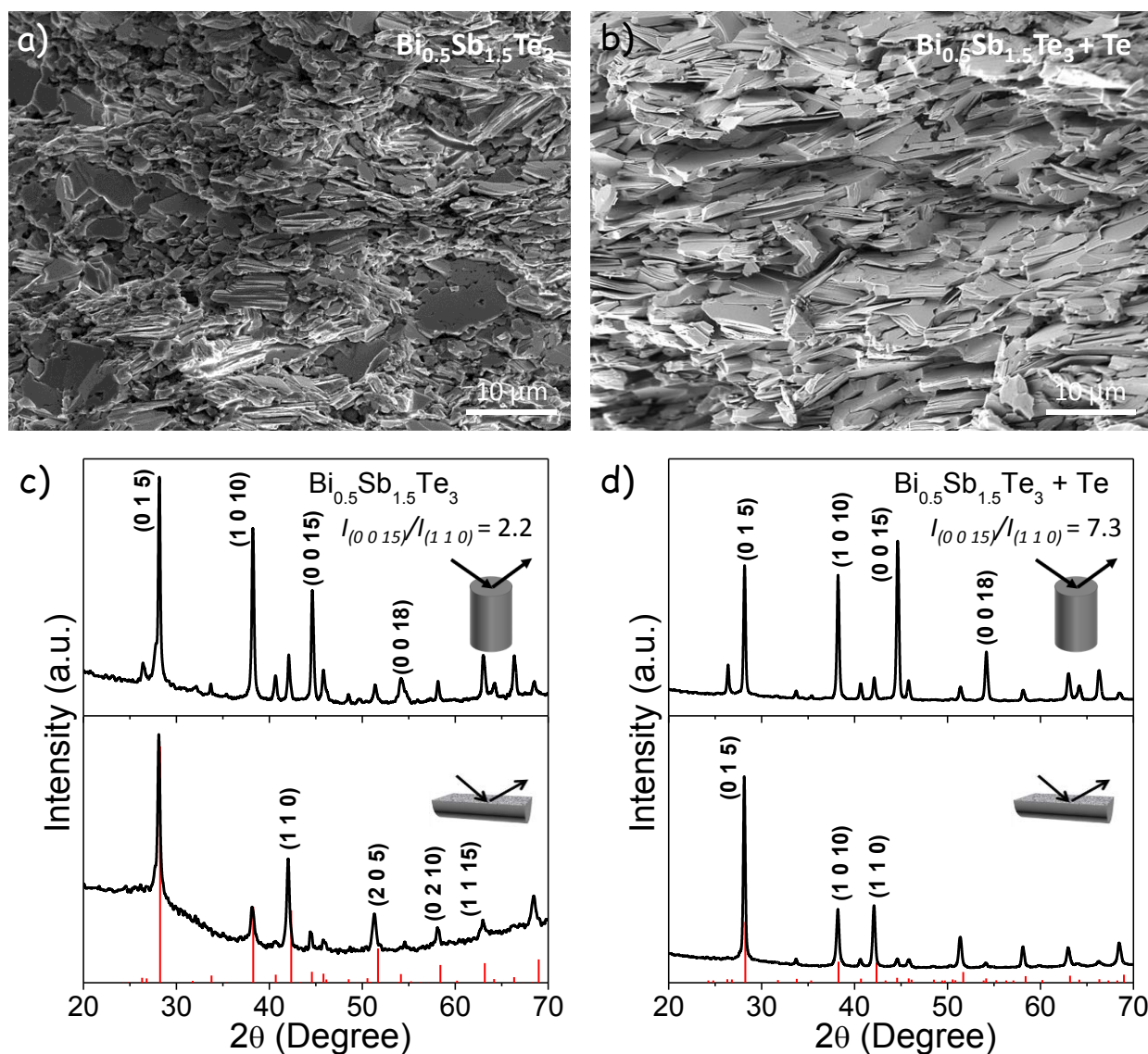


**Figure S7.** a-b) Cross-section SEM micrographs of the  $\text{Bi}_{0.5}\text{Sb}_{1.5}\text{Te}_3$  pellets produced without (a) and with (b) an excess of tellurium in the initial nanoplatelets. c) and d) XRD pattern of the  $\text{Bi}_{0.5}\text{Sb}_{1.5}\text{Te}_3$  pellet produced without and with an excess of tellurium, respectively. Red vertical lines correspond to the reference literature data for  $\text{Sb}_2\text{Te}_3$ , JCPDS NO. 01-071-0393.

### 13. $\text{Bi}_2\text{Te}_3$ nanowires as initial building blocks

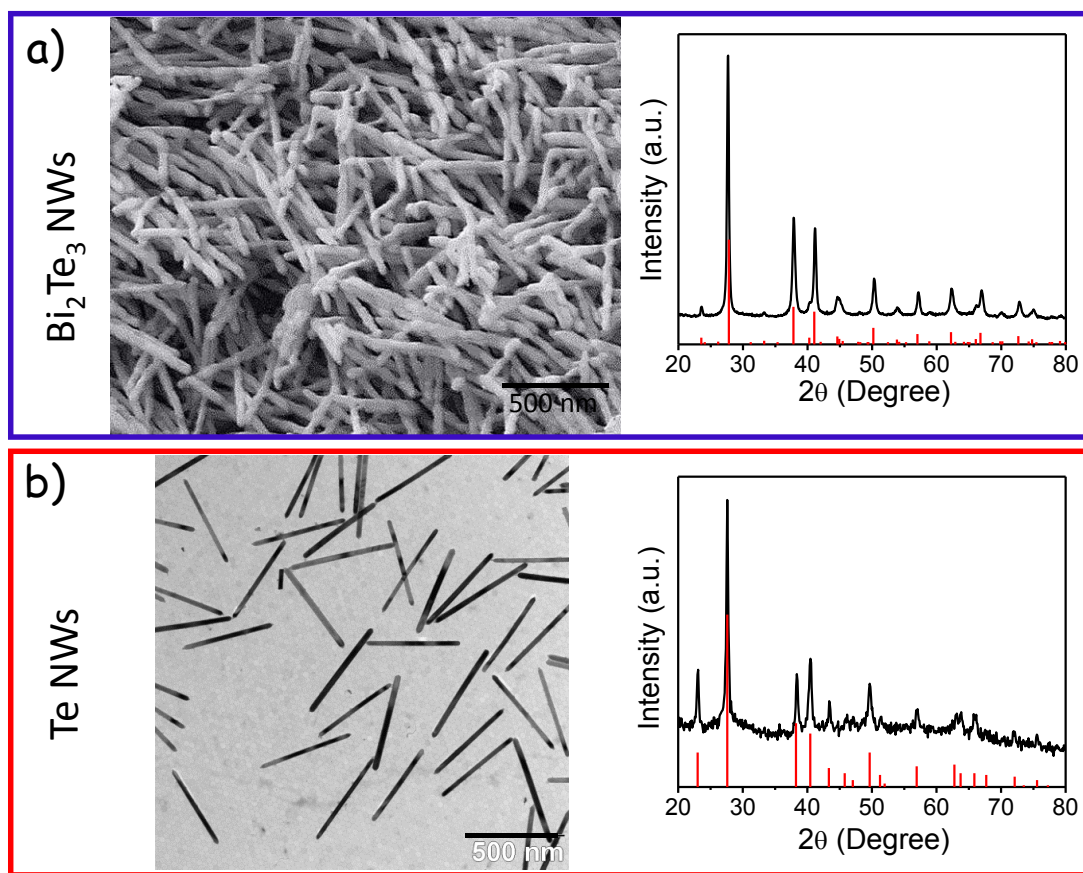


**Figure S8.** a) Representative SEM micrograph of  $\text{Bi}_2\text{Te}_3$  nanowires and the corresponding XRD pattern including a  $\text{Bi}_2\text{Te}_3$  reference (JCPDS NO. 01-089-2009). b) TEM micrograph of tellurium nanowires and the corresponding XRD pattern, including a tellurium reference (JCPDS NO. 00-004-0555).

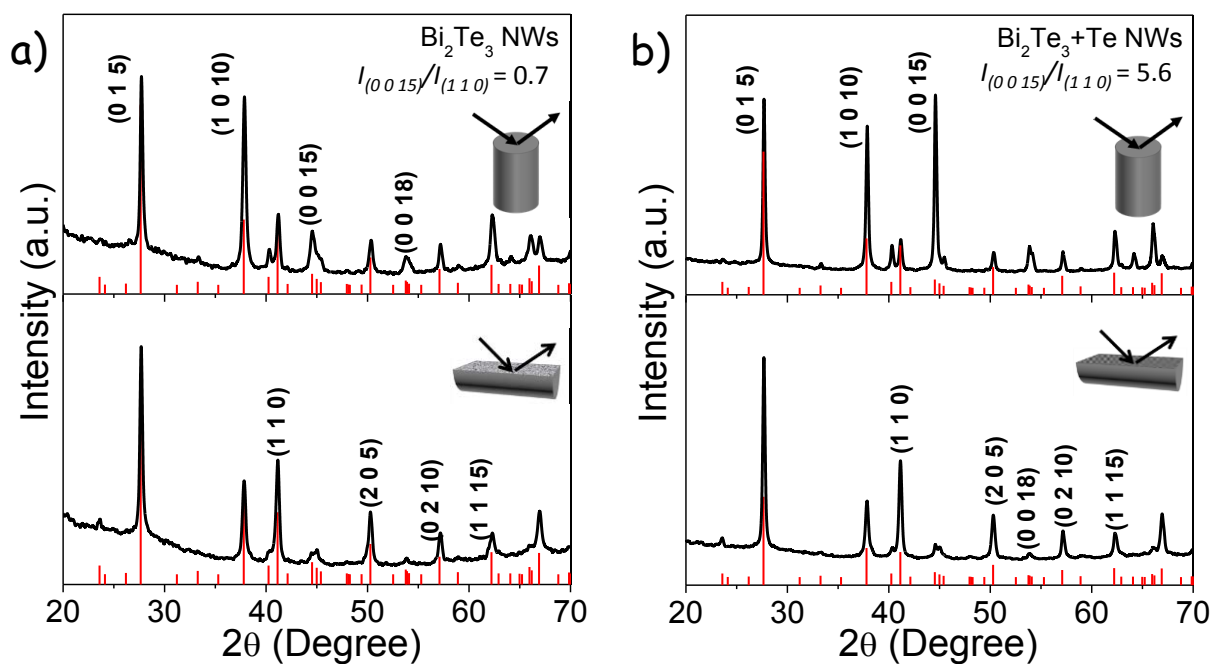


**Figure S9.** XRD patterns of the  $\text{Bi}_2\text{Te}_3$  (a) and  $\text{Bi}_2\text{Te}_3+\text{Te}$  (b) pellets placed to have the x-ray diffraction plane in two perpendicular directions as marked within the graph. Pellets were consolidated by hot pressing the nanowires at 480 °C for 210 s. Red vertical lines correspond to the reference literature data for  $\text{Bi}_2\text{Te}_3$ , JCPDS NO. 01-089-2009.

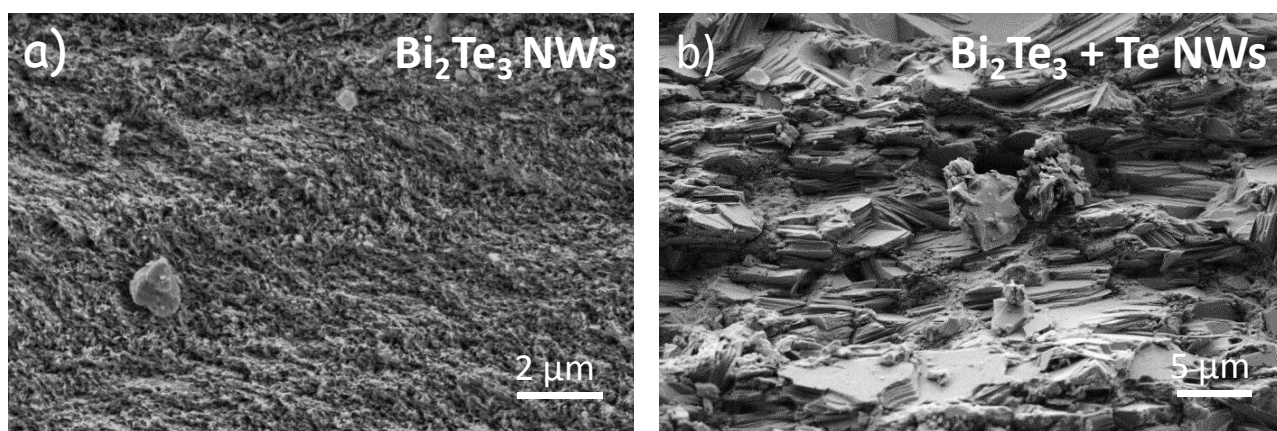


**Figure S10.** Cross-section SEM micrographs of  $\text{Bi}_2\text{Te}_3$  (a) and  $\text{Bi}_2\text{Te}_3+\text{Te}$  (b) nanowires hot-pressed at 480 °C.



#### 14. Commercial $\text{Bi}_{0.5}\text{Sb}_{1.5}\text{Te}_3$ ingot

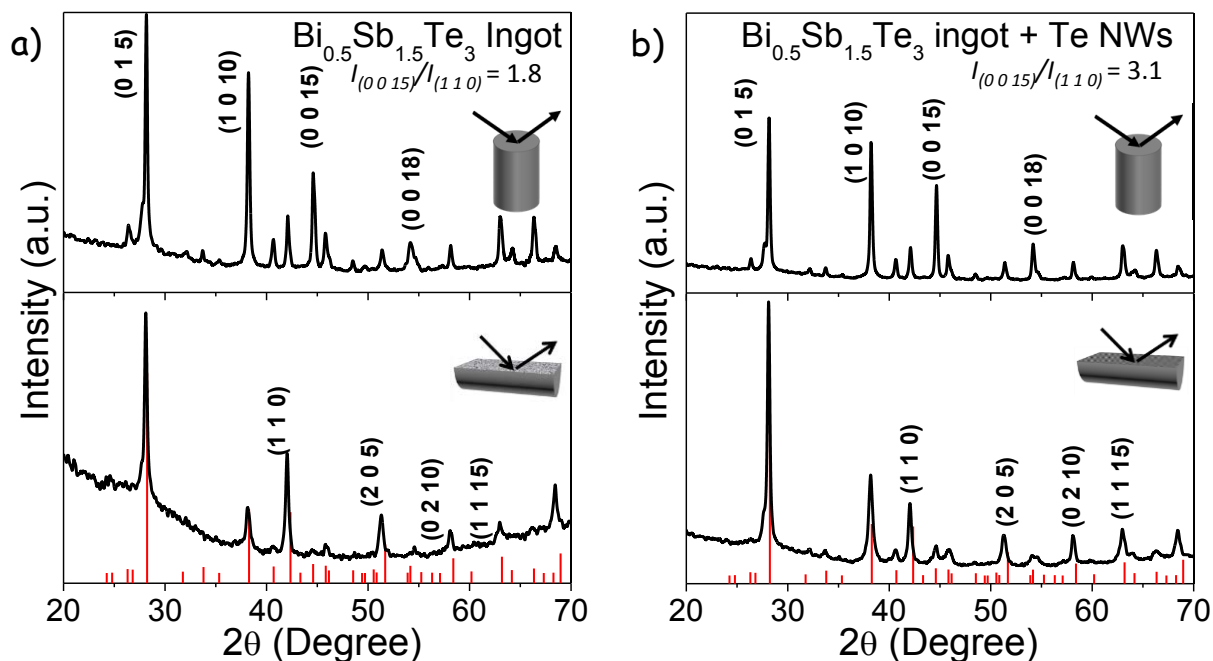


**Figure S11.** XRD patterns of a ball milled and later consolidated (hot press at 480 °C during 210 s) commercial ingot. a) Pellet produced from the consolidation of a  $\text{Bi}_{0.5}\text{Sb}_{1.5}\text{Te}_3$  nanopowder obtained by ball milling a commercial ingot. b) Pellet produced from the consolidation of a  $\text{Bi}_{0.5}\text{Sb}_{1.5}\text{Te}_3 + \text{Te}$  nanopowder obtained by ball milling a commercial ingot and adding tellurium nanowires to it. Red vertical lines correspond to the reference literature data for  $\text{Sb}_2\text{Te}_3$ , JCPDS NO. 01-071-0393.

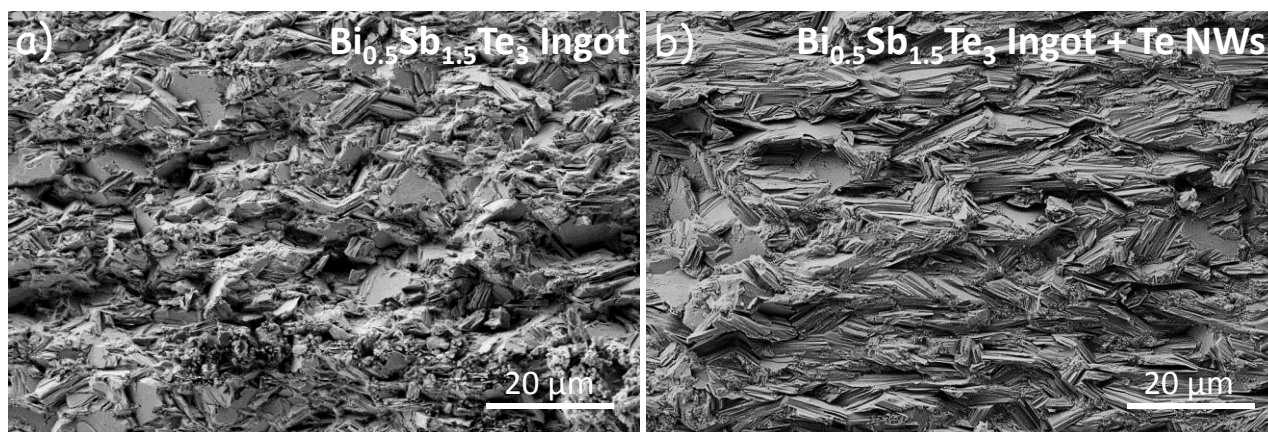


**Figure S12.** Cross-section SEM micrographs of a ball milled and later consolidated (hot press at 480 °C during 210 s) commercial ingot. a) Pellet produced from the consolidation of a  $\text{Bi}_{0.5}\text{Sb}_{1.5}\text{Te}_3$  nanopowder obtained by ball milling a commercial ingot. b) Pellet produced from the consolidation of a  $\text{Bi}_{0.5}\text{Sb}_{1.5}\text{Te}_3 + \text{Te}$  nanopowder obtained by ball milling a commercial ingot and adding tellurium nanowires to it.

## 15. Tellurium spilling

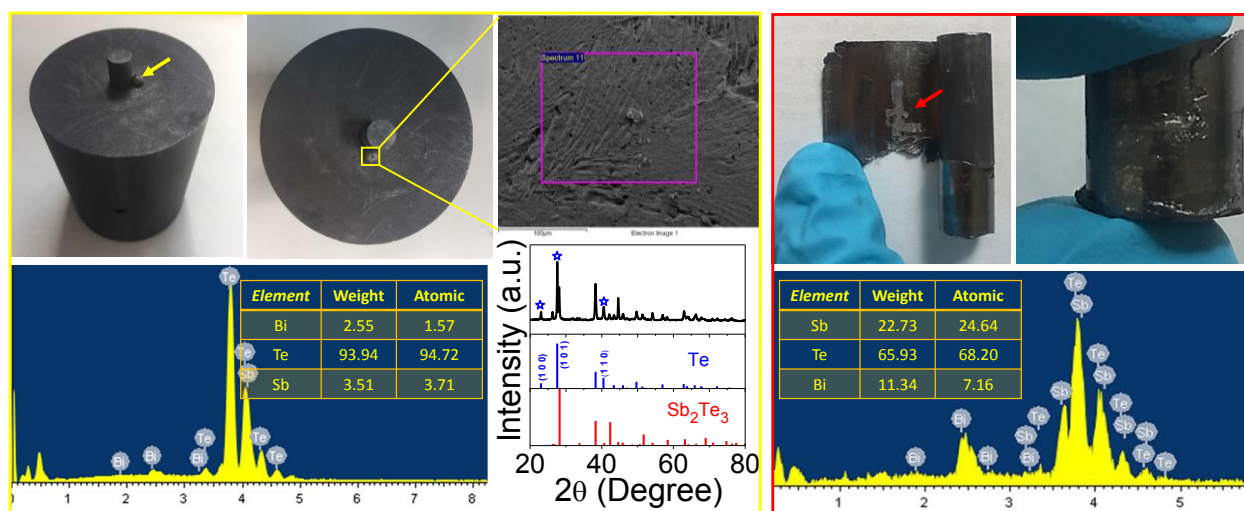


**Figure S13.** Photographs of the graphite dies and the carbon rod covered with a graphite foil after hot press. As indicated by the yellow and red arrows, some material was expelled out from the graphite die during the hot press. XRD and EDX analysis of the material spilled out confirming that between 70-90% of this material is tellurium.

## 16. One press and release step

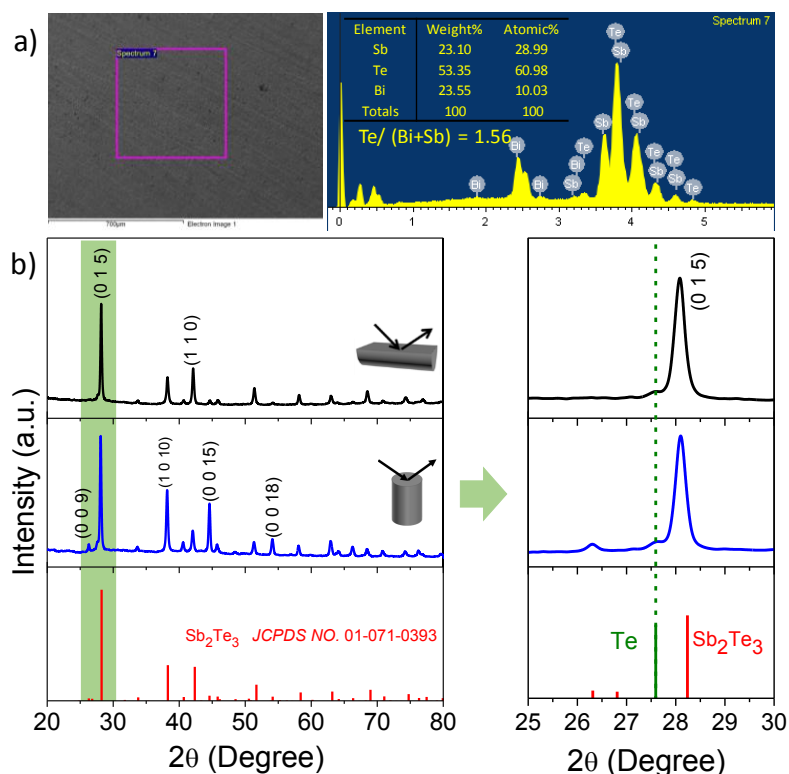


**Figure S14.** a) SEM micrograph and SEM-EDX composition of a  $\text{Bi}_{0.5}\text{Sb}_{2.5}\text{Te}_3 + \text{Te}$  pellet hot pressed at  $480^\circ\text{C}$  for 210 s using just one pressure and release step. b) XRD patterns of the same pellet showing the presence of a weak tellurium peak at  $27.5^\circ$ , according to the tellurium reference pattern JCPDS NO. 00-004-0554.



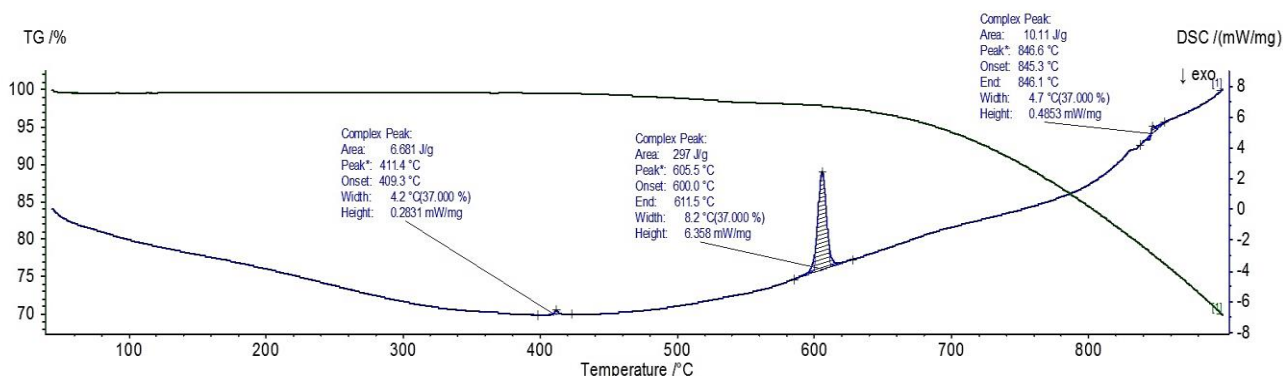


**Figure S15.** TGA-DSC of a  $\text{Bi}_{0.5}\text{Sb}_{2.5}\text{Te}_3+\text{Te}$  pellet hot pressed at 480 °C for 210 s using just one pressure and release step. Besides the large exothermic peak at 605 °C associated to the melting of the  $\text{Bi}_{0.5}\text{Sb}_{2.5}\text{Te}_3$  alloy, a weak exothermic peak at ~411 °C associated to a tellurium-rich phase is observed.

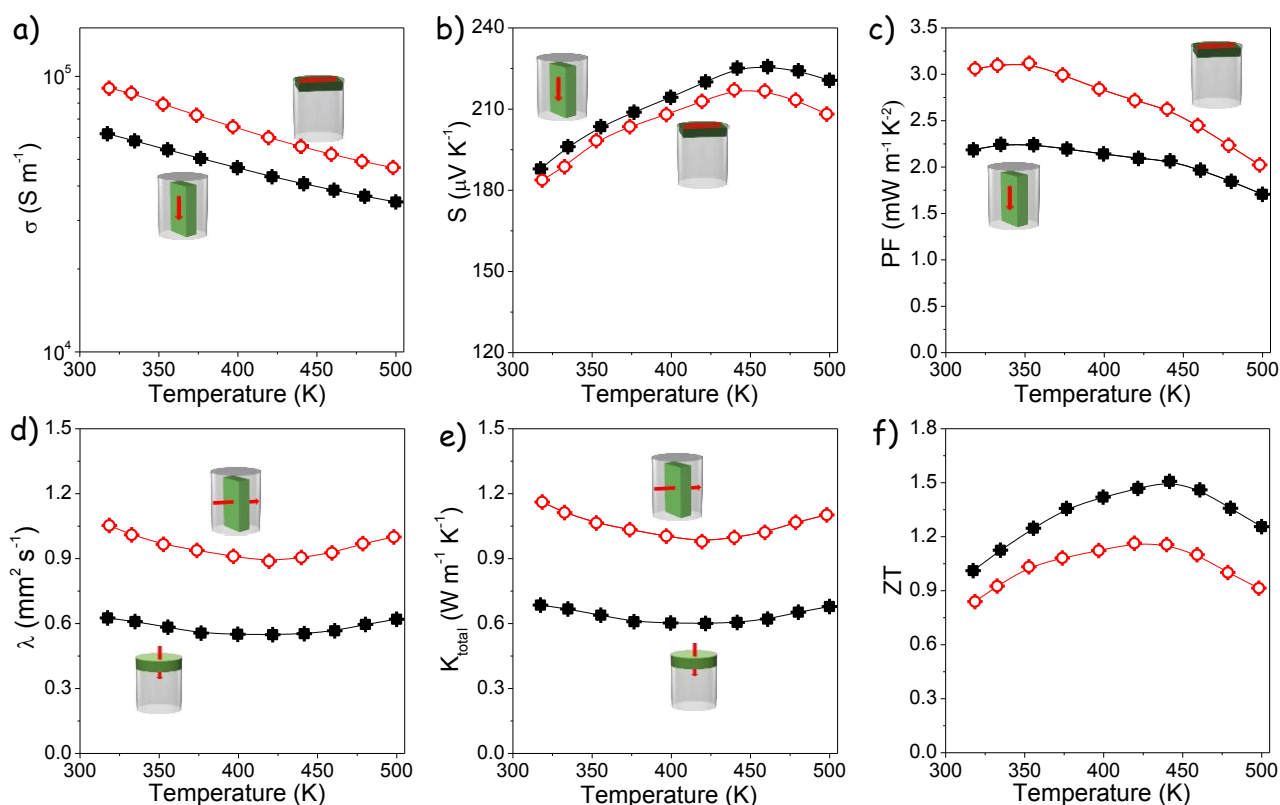


**Figure S16.** Temperature dependence of electric conductivity,  $\sigma$  (a); Seebeck coefficient,  $S$  (b); power factor, PF (c); thermal diffusivity,  $\lambda$  (d); thermal conductivity,  $\kappa_{\text{total}}$  (e); and thermoelectric figure of merit, ZT (f) of the  $\text{Bi}_{0.5}\text{Sb}_{2.5}\text{Te}_3+\text{Te}$  pellet hot pressed at 480 °C for 210 s using just one pressure and release step.

## 17. Composition optimization

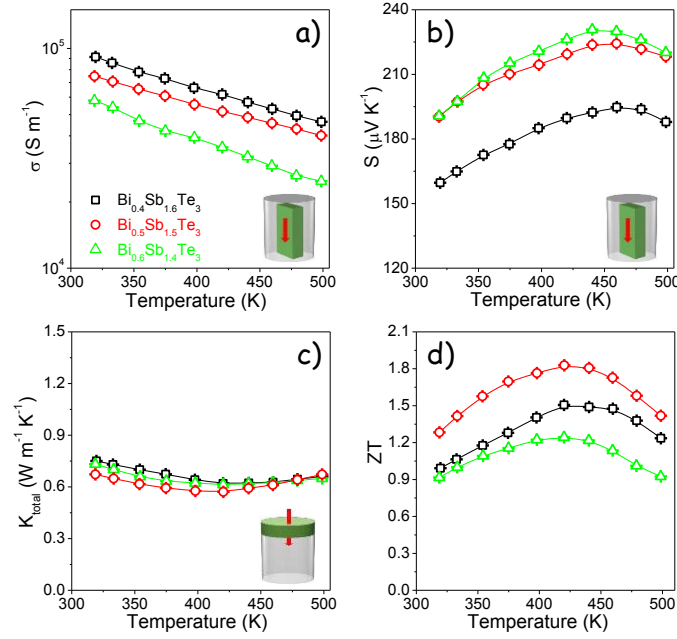


**Figure S17.** Temperature dependence of electric conductivity,  $\sigma$  (a); Seebeck coefficient,  $S$  (b); thermal conductivity,  $\kappa_{\text{total}}$  (c); and thermoelectric figure of merit,  $ZT$  (d) of  $\text{Bi}_x\text{Sb}_{2-x}\text{Te}_3$  (x=0.4, 0.5 and 0.6) samples measured in the direction parallel to the press axis. The plotted data values were obtained by averaging the experimental data measured from five samples having approximately the same composition.

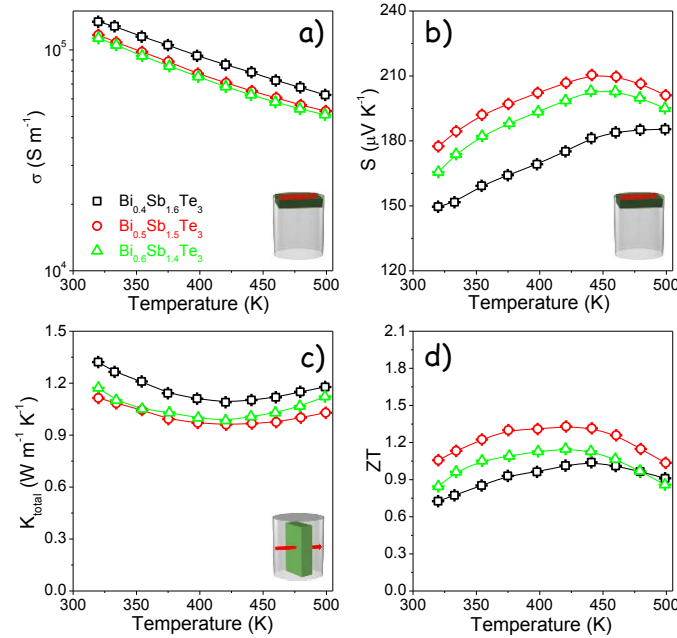


**Figure S18.** Temperature dependence of electric conductivity,  $\sigma$  (a); Seebeck coefficient,  $S$  (b); thermal conductivity,  $\kappa_{\text{total}}$  (c); and thermoelectric figure of merit,  $ZT$  (d) of  $\text{Bi}_x\text{Sb}_{2-x}\text{Te}_3$  (x=0.4, 0.5 and 0.6) samples measured in the plane normal to the press axis. The plotted data values were obtained by averaging the experimental data measured from five samples having approximately the same composition.

## 18. Additional thermoelectric properties

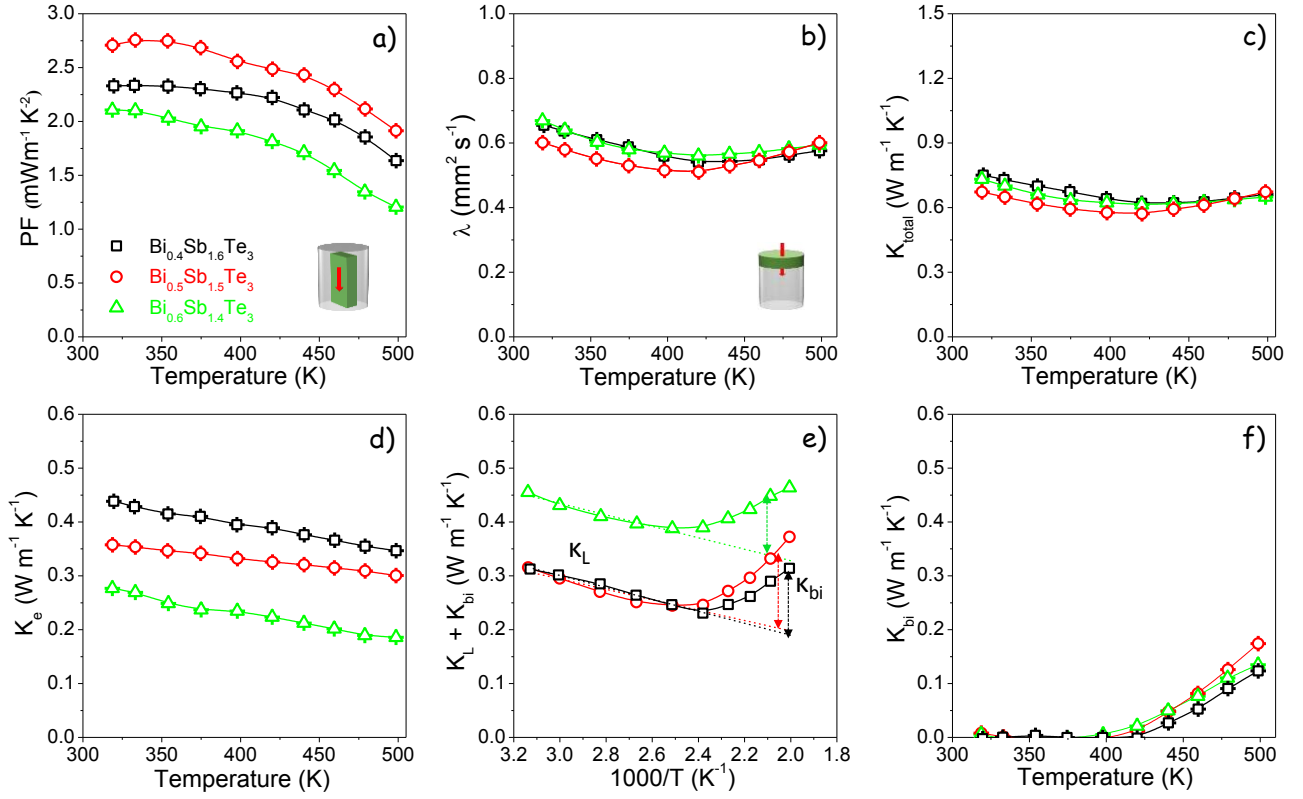


**Figure S19.** Temperature dependence of the power factor, PF (a); thermal diffusivity,  $\lambda$  (b); thermal conductivity,  $\kappa_{\text{total}}$  (c); electronic component to the thermal conductivities,  $\kappa_e$  (d); lattice and bipolar thermal conductivities,  $\kappa_L + \kappa_{\text{bi}}$  (e), and bipolar component to the thermal conductivity,  $\kappa_{\text{bi}}$ , estimated as the difference between  $\kappa_{\text{total}} - \kappa_e$  and a linear fitting of  $\kappa_{\text{total}} - \kappa_e$  as a function of  $1/T$  in the low temperature range (f) of  $\text{Bi}_x\text{Sb}_{2-x}\text{Te}_3$  (x=0.4, 0.5, and 0.6) measured in the direction of the press axis. The plotted data values were obtained by averaging the experimental data measured from five samples having approximately the same composition.

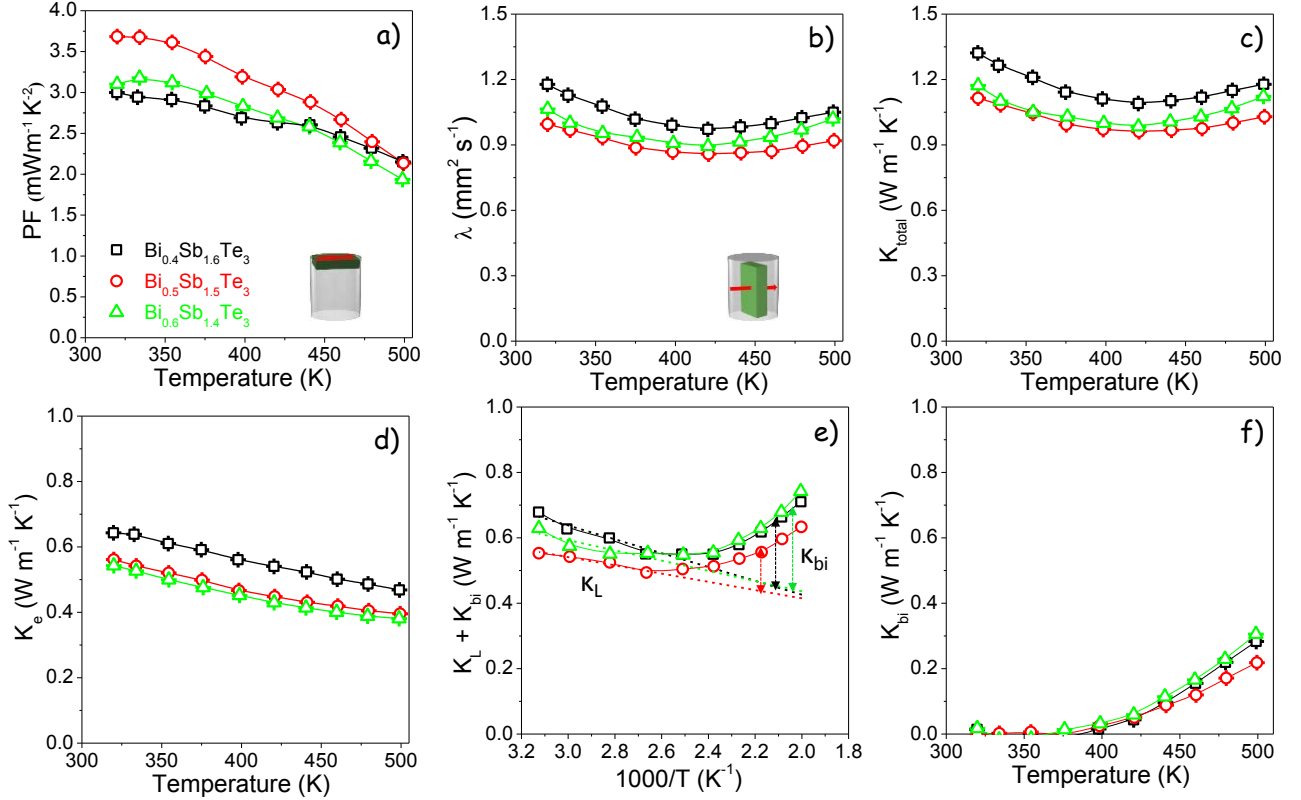


**Figure S20.** Temperature dependence of the power factor, PF (a); thermal diffusivity,  $\lambda$  (b); thermal conductivity,  $\kappa_{\text{total}}$  (c); electronic component to the thermal conductivities,  $\kappa_e$  (d); lattice and bipolar thermal conductivities,  $\kappa_L + \kappa_{\text{bi}}$  (e), and bipolar component to the thermal conductivity,  $\kappa_{\text{bi}}$ , estimated as the difference between  $\kappa_{\text{total}} - \kappa_e$  and a linear fitting of  $\kappa_{\text{total}} - \kappa_e$  as a function of  $1/T$  in the low temperature range (f) of  $\text{Bi}_x\text{Sb}_{2-x}\text{Te}_3$  ( $x=0.4, 0.5$ , and  $0.6$ ) measured in the plane normal to the press axis. The plotted data values were obtained by averaging the experimental data measured from five samples having approximately the same composition.

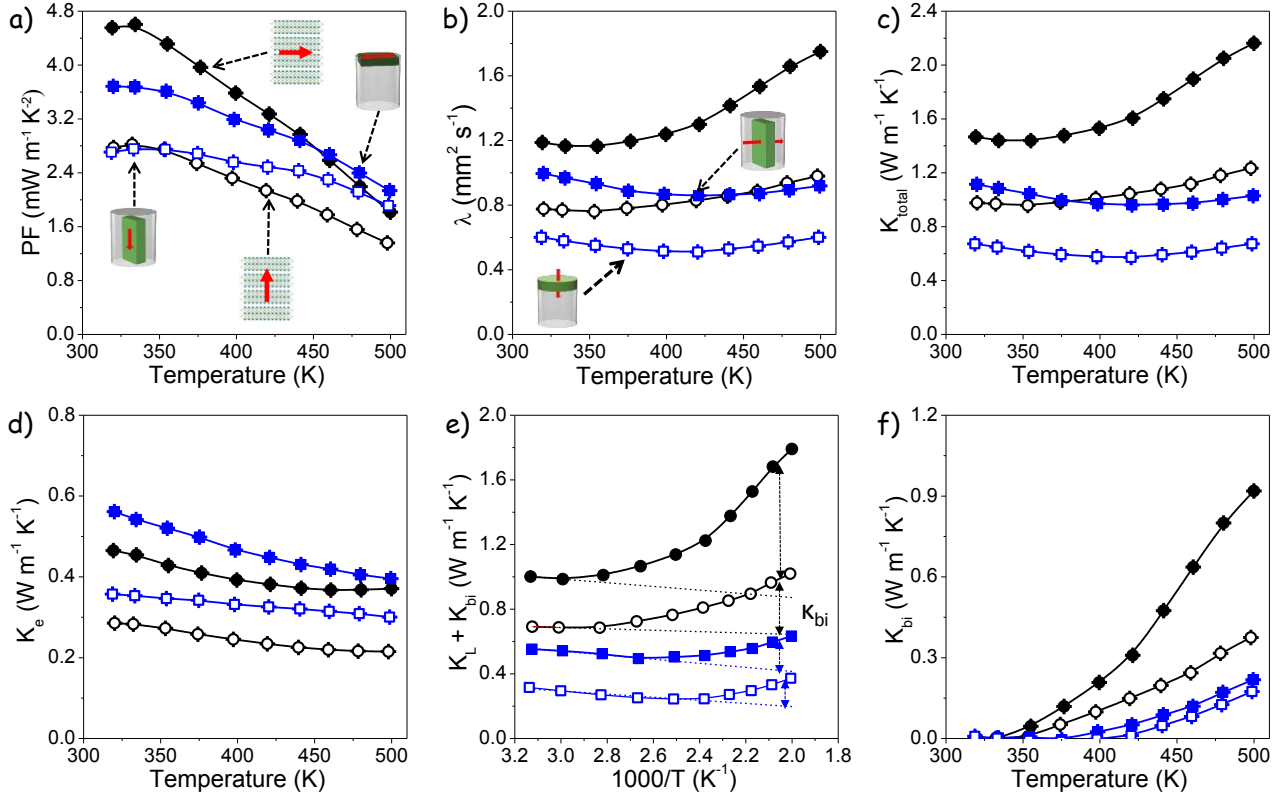


**Figure S21.** Temperature dependence of the power factor, PF (a); thermal diffusivity,  $\lambda$  (b); thermal conductivity,  $\kappa_{\text{total}}$  (c); electronic component to the thermal conductivities,  $\kappa_e$  (d); lattice and bipolar thermal conductivities,  $\kappa_L + \kappa_{bi}$  (e), and bipolar component to the thermal conductivity,  $\kappa_{bi}$ , estimated as the difference between  $\kappa_{\text{total}} - \kappa_e$  and a linear fitting of  $\kappa_{\text{total}} - \kappa_e$  as a function of  $1/T$  in the low temperature range (f) of the nanomaterial and the commercial sample. The  $\text{Bi}_{0.5}\text{Sb}_{1.5}\text{Te}_3$  nanomaterial hot pressed at 480 °C (blue squares) was measured in two directions, parallel (open squares) and normal (solid squares) to the press axis. The plotted data were obtained by averaging the experimental data measured from five samples having approximately the same composition. The commercial ingot (black circles) was measured in two directions, parallel (solid circles) and normal (open circles) to the cleavage direction.



### 19. Average values and maximum efficiency

Average ZT values were calculated in the range from 320 K to 500 K by integrating the ZT values curve interpolated with a spline function and dividing the obtained area by the temperature difference (180 K). For this calculated we used the mean values from the experimental data measured from five samples having approximately the same composition.

$$ZT_{ave} = \frac{\int_{T_0}^{T_f} ZT dT}{\Delta T}$$

From this calculation, the average ZT obtained in the *c* direction from the bottom-up nanomaterial was:

$$ZT_{ave}=1.65.$$

The average ZT obtained from the commercial sample was:

$$ZT_{ave}=0.84$$

The maximum efficiency based on cumulative temperature-dependent properties was calculated from:<sup>5, 6</sup>

$$\eta_{max} = \eta_c \frac{\sqrt{1 + ZT_{eng}(\alpha/\eta_c - 1/2)} - 1}{\alpha \left( \sqrt{1 + ZT_{eng}(\alpha/\eta_c - 1/2)} + 1 \right) - \eta_c}$$

with

$$ZT_{eng} = \frac{\left( \int_{T_c}^{T_h} S(T) dT \right)^2}{\int_{T_c}^{T_h} \rho(T) dT \int_{T_c}^{T_h} \kappa(T) dT} \Delta T$$

$$\eta_c = \frac{T_h - T_c}{T_h}$$

$$\alpha = \frac{S(T_h) \Delta T}{\int_{T_c}^{T_h} S(T) dT}$$

From these equations, the maximum efficiency obtained in the *c* direction from the bottom-up nanomaterial considering  $T_h=500$  K and  $T_c=320$  K was:

$$\eta_{max} = 10.4 \text{ \%}.$$

The maximum efficiency from the commercial sample considering  $T_h=500$  K and  $T_c=320$  K was:

$$\eta_{max} = 7.1 \text{ \%}$$

## 20. Literature comparison

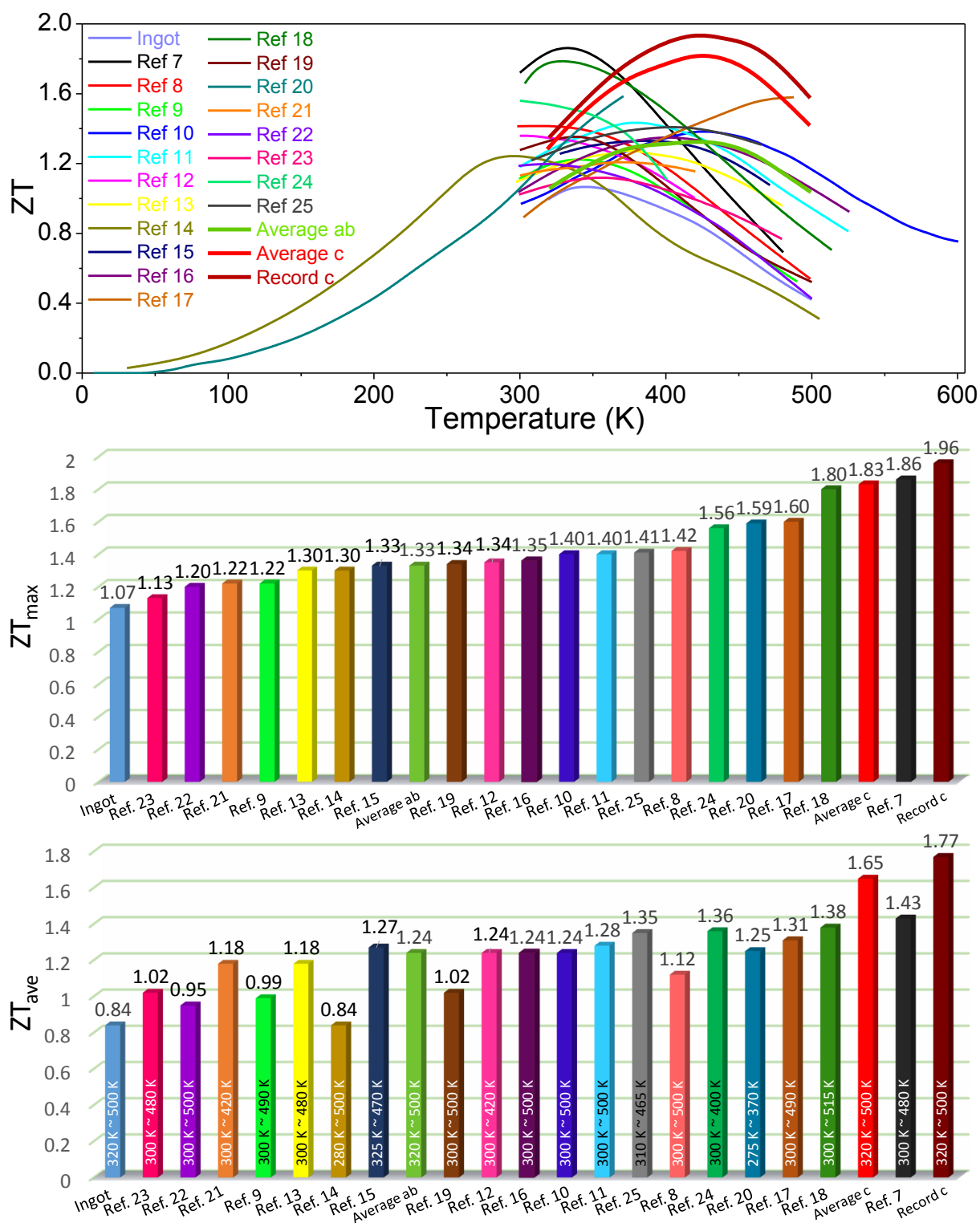


**Figure S22.** State-of-the-art ZT values and average ZT values for p-type  $\text{Bi}_2\text{Te}_3$ -based alloys.<sup>7-25</sup> Our data is named as “average ab”, “average c” and “record c”, corresponding to the values obtained from averaging the experimental data measured from five different samples in the two directions (perpendicular (ab) and parallel (c) to the press axis), and to the record materials (among the five samples) measured in the direction parallel to the press axis, respectively.

## 21. Stability

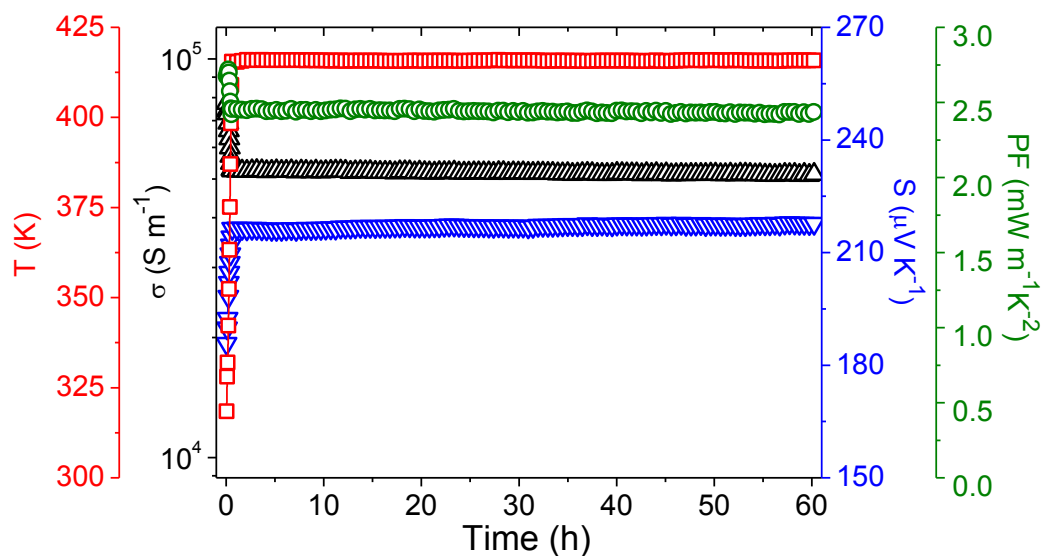


**Figure S23.** Time evolution of the electric conductivity ( $\sigma$ ), Seebeck coefficient ( $S$ ), power factor ( $\text{PF}$ ) and temperature ( $T$ ) of  $\text{Bi}_{0.5}\text{Sb}_{1.5}\text{Te}_3$  during a 60 h test.

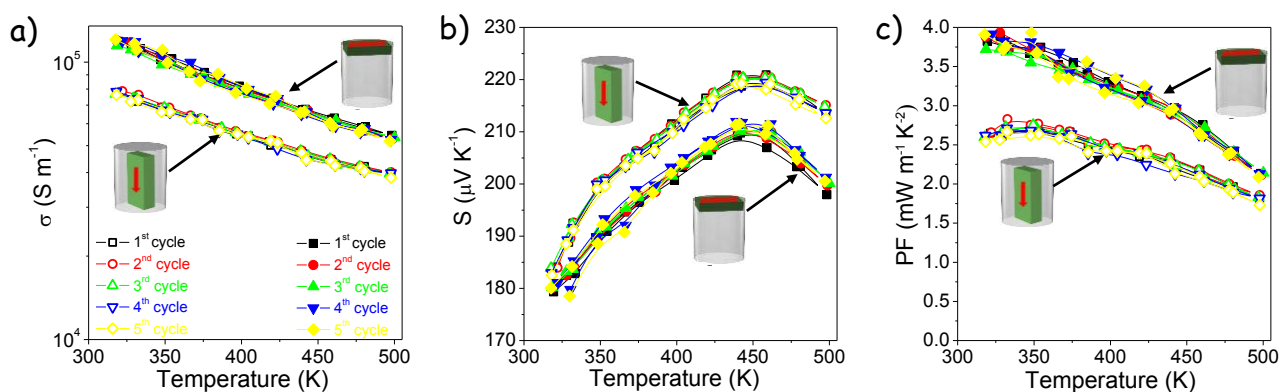


**Figure S24.** Temperature dependence of the electrical conductivity,  $\sigma$  (a), Seebeck coefficient,  $S$  (b), and power factor,  $\text{PF}$  (c) of  $\text{Bi}_{0.5}\text{Sb}_{1.5}\text{Te}_3$  pellets measured in 5 consecutive up-down cycles during the heating up from room temperature to 498 K. No pre-stabilization treatment was carried out before the first measurement.

## 22. Repeatability

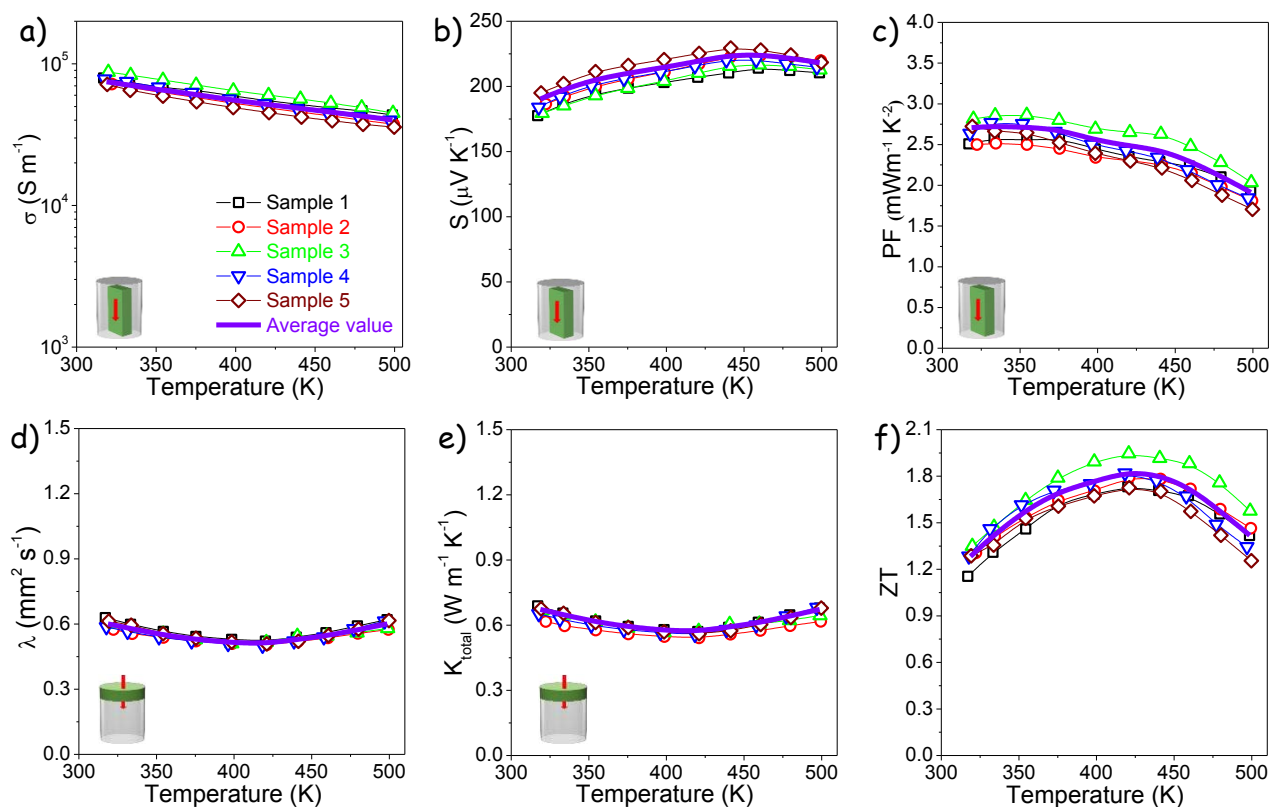


**Figure S25.** Temperature dependence of electric conductivity,  $\sigma$  (a); Seebeck coefficient,  $S$  (b); power factor, PF (c); thermal diffusivity,  $\lambda$  (d); thermal conductivity,  $\kappa_{\text{total}}$  (e); and thermoelectric figure of merit, ZT (f) of five  $\text{Bi}_{0.5}\text{Sb}_{1.5}\text{Te}_3$  pellets measured in the direction parallel to the press axis. The violet line corresponds to the average value obtained from the five samples.

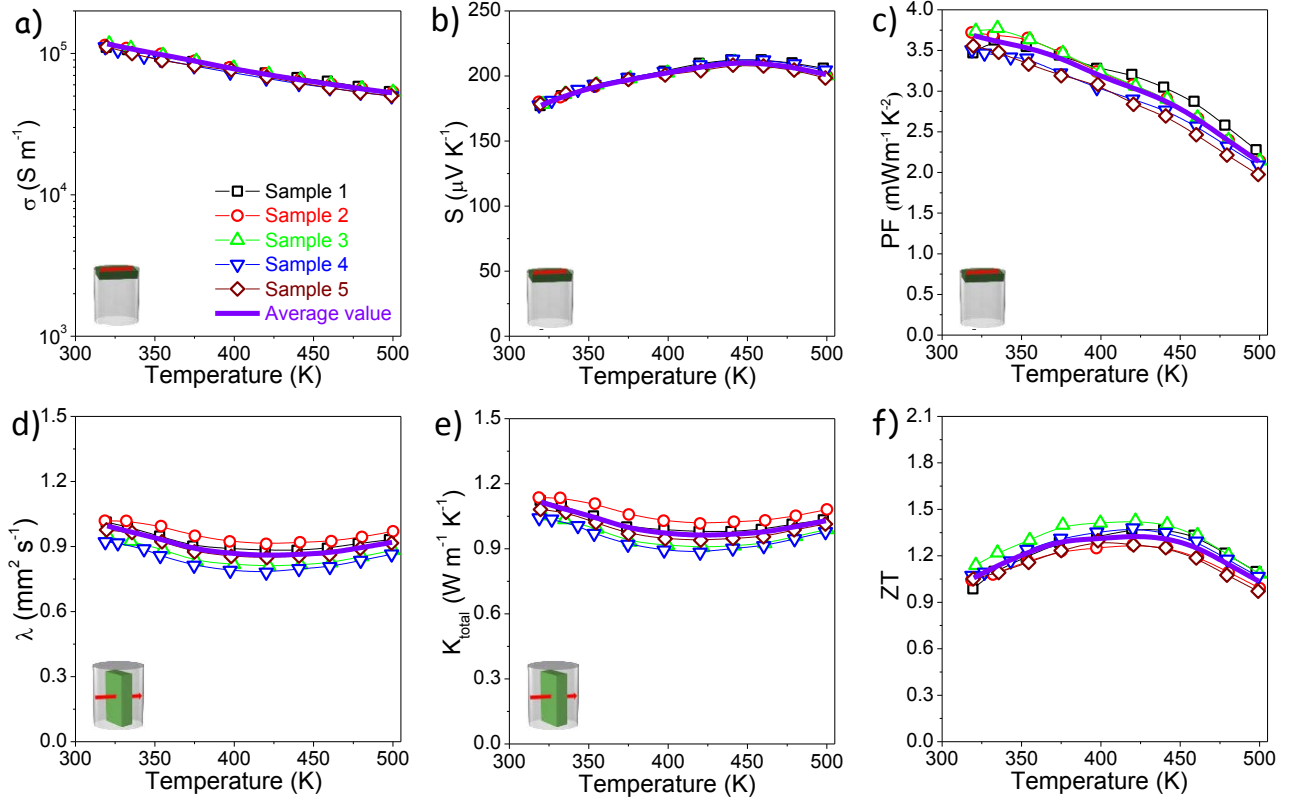


**Figure S26.** Temperature dependence of electric conductivity,  $\sigma$  (a); Seebeck coefficient,  $S$  (b); power factor, PF (c); thermal diffusivity,  $\lambda$  (d); thermal conductivity,  $\kappa_{\text{total}}$  (e); and thermoelectric figure of merit, ZT (f) of the  $\text{Bi}_{0.5}\text{Sb}_{1.5}\text{Te}_3$  pellet measured in the plane normal to the press axis. The violet line corresponds to the average value obtained from the five samples.



## 23. References

1. G. Zhang, B. Kirk, L. A. Jauregui, H. Yang, X. Xu, Y. P. Chen and Y. Wu, *Nano Lett.*, 2011, **12**, 56-60.
2. N. Serebryanaya, E. Tatyannin, S. Buga, I. Kruglov, N. Lvova and V. Blank, *Phys. Status Solidi B*, 2015, **252**, 267-273.
3. Y. Zhao, M. de la Mata, R. L. Qiu, J. Zhang, X. Wen, C. Magen, X. P. Gao, J. Arbiol and Q. Xiong, *Nano Res.*, 2014, **7**, 1243-1253.
4. C. Chen, B. Zhang, D. Liu and Z. Ge, *Intermetallics*, 2012, **25**, 131-135.
5. H. S. Kim, W. Liu and Z. Ren, *Energy Environ. Sci.*, 2017, **10**, 69-85.
6. H. S. Kim, W. Liu, G. Chen, C.-W. Chu and Z. Ren, *Proc. Natl. Acad. Sci. U.S.A.*, 2015, **112**, 8205-8210.
7. S. I. Kim, K. H. Lee, H. A. Mun, H. S. Kim, S. W. Hwang, J. W. Roh, D. J. Yang, W. H. Shin, X. S. Li and Y. H. Lee, *Science*, 2015, **348**, 109-114.
8. Y. Yu, D.-S. He, S. Zhang, O. Cojocaru-Mirédin, T. Schwarz, A. Stoffers, X.-Y. Wang, S. Zheng, B. Zhu and C. Scheu, *Nano Energy*, 2017, **37**, 203-213.
9. Y. Zheng, Q. Zhang, X. Su, H. Xie, S. Shu, T. Chen, G. Tan, Y. Yan, X. Tang and C. Uher, *Adv. Energy Mater.*, 2015, **5**, 1401391.
10. F. Hao, P. Qiu, Q. Song, H. Chen, P. Lu, D. Ren, X. Shi and L. Chen, *Materials*, 2017, **10**, 251.
11. B. Poudel, Q. Hao, Y. Ma, Y. Lan, A. Minnich, B. Yu, X. Yan, D. Wang, A. Muto and D. Vashaee, *Science*, 2008, **320**, 634-638.
12. X. Tang, W. Xie, H. Li, W. Zhao, Q. Zhang and M. Niino, *Appl. Phys. Lett.*, 2007, **90**, 012102.
13. L.-P. Hu, T.-J. Zhu, Y.-G. Wang, H.-H. Xie, Z.-J. Xu and X.-B. Zhao, *NPG Asia Mater.*, 2014, **6**, e88.
14. T. Zhu, Z. Xu, J. He, J. Shen, S. Zhu, L. Hu, T. M. Tritt and X. Zhao, *J. Mater. Chem. A*, 2013, **1**, 11589-11594.
15. J. Li, Q. Tan, J. F. Li, D. W. Liu, F. Li, Z. Y. Li, M. Zou and K. Wang, *Adv. Funct. Mater.*, 2013, **23**, 4317-4323.
16. Z. Xu, L. Hu, P. Ying, X. Zhao and T. Zhu, *Acta Mater.*, 2015, **84**, 385-392.
17. Y. Li, X. Qin, D. Li, J. Zhang, C. Li, Y. Liu, C. Song, H. Xin and H. Guo, *Appl. Phys. Lett.*, 2016, **108**, 062104.
18. S. Fan, J. Zhao, J. Guo, Q. Yan, J. Ma and H. H. Hng, *Appl. Phys. Lett.*, 2010, **96**, 182104.
19. B. Madavali, H. Kim, K. Lee and S. Hong, *J. Appl. Phys.*, 2017, **121**, 225104.
20. C. Zhang, M. de la Mata, Z. Li, F. J. Belarre, J. Arbiol, K. A. Khor, D. Poletti, B. Zhu, Q. Yan and Q. Xiong, *Nano Energy*, 2016, **30**, 630-638.
21. R. J. Mehta, Y. Zhang, C. Karthik, B. Singh, R. W. Siegel, T. Borca-Tasciuc and G. Ramanath, *Nat. Mater.*, 2012, **11**, 233-240.
22. M. Hong, Z. G. Chen, L. Yang and J. Zou, *Nano Energy*, 2016, **20**, 144-155.
23. D. Suh, S. Lee, H. Mun, S.-H. Park, K. H. Lee, S. W. Kim, J.-Y. Choi and S. Baik, *Nano Energy*, 2015, **13**, 67-76.
24. W. Xie, X. Tang, Y. Yan, Q. Zhang and T. M. Tritt, *Appl. Phys. Lett.*, 2009, **94**, 102111.
25. Y. M. Kim, R. Lydia, J.-H. Kim, C.-C. Lin, K. Ahn and J.-S. Rhyee, *Acta Mater.*, 2017, **135**, 297-303.